Supporting Information for

Towards a Rational Design of Bioactive Glasses with Optimal Structural Features: Composition-Structure Correlations Unveiled by Solid-State NMR and MD Simulations

Renny Mathew[a], Baltzar Stevensson[a], Antonio Tilocca[b], and Mattias Edén[a,*]

[a]Physical Chemistry Division, Department of Materials and Environmental Chemistry, Arrhenius Laboratory, Stockholm University, SE-106 91 Stockholm, Sweden
[b]Department of Chemistry and Thomas Young Centre for the Theory and Simulations of Materials, University College London, London WC1H 0AJ, U.K.

*Corresponding author. E-mail: *mattias.eden@mmk.su.se*

Contents

S1 ^{31}P NMR

S1.1 Spectra Deconvolutions

The deconvolutions of the ^{31}P NMR spectra employed relatively constrained parameter spaces within each fixed-$\overline{N}^{\mathrm{Si}}_{\mathrm{BO}}$ series: each value of the chemical shift (δ^n_{P}) and the fwhm height (W^n_{P}) was restricted within $\pm$1 ppm and $\pm$2 ppm, respectively. Such a procedure ensures consistency in the data fitting. Yet, generally the resulting best-fit fractional populations did not differ substantially from those extracted by using unconstrained $\{\delta^n_{\mathrm{P}},\ W^n_{\mathrm{P}}\}$ parameters during the fitting. The latter approach reduced the root-mean-square (rms) deviations to the experiments marginally (typically by 20%), while sometimes producing physically dubious values of the chemical shift or peakwidth of the minor Q^1_{P} signal. Regardless of the precise restrictions imposed on the $\{\delta^n_{\mathrm{P}},\ W^n_{\mathrm{P}}\}$ ranges, a near-constancy of the $\{x^0_{\mathrm{P}},\ x^1_{\mathrm{P}}\}$ fractions was observed among the glasses with a (nearly) fixed silicate network connectivity.

Besides the ^{31}P NMR centerband peaks shown in the zoomed spectra of Figs. 1 and 2, the reported fractional populations (x^n_{P}) accounts for the contributions from spinning sidebands arising at the relatively low MAS rate of 7.0 kHz employed herein; they are visible in Fig. S1 that plots a selection of ^{31}P NMR spectra over a larger ppm range. Owing to the comparatively high ^{31}P chemical shift anisotropy (CSA) of the less symmetric Q^1_{P} environments relative to their Q^0_{P} counterparts,[S1–S3] around 30% and 10% of each respective total NMR signal intensity is concentrated in the sidebands. We refer to Leonova *et al.*[S2] for discussions on the relative ^{31}P CSA magnitudes of Q^0_{P} and Q^1_{P} groups. The accuracy of the iterative fitting improved by exploiting the readily identified ^{31}P NMR peak positions of the Q^1_{P} groups at the left and right spinning sidebands to constrain the δ^1_{P} chemical shift at the centerpeak, whose ^{31}P NMR signal is otherwise masked by the more intense one from the Q^0_{P} species (see Fig. S1).

Furthermore, inspecting the spinning sideband *peakshapes* assists the *detection* of the Q^1_{P} moieties, particularly for glasses featuring low silicate network connectivities $\overline{N}^{\mathrm{Si}}_{\mathrm{BO}} \approx 2.1$, and thereby very modest fractional populations $x^1_{\mathrm{P}} \approx 0.05$, such as in the "45S5" structure; see Table 2. In such cases, the Q^1_{P} signals cannot be unambiguously identified if only considering the region around the central ^{31}P MAS NMR resonances. Hence, based on the centerband signal alone, there is no strong justification for involving a second NMR peak from Q^1_{P} groups in the deconvolution. Yet, a very high signal-to-noise (S/N) ratio is required to allow analysis of the much weaker sidebands: for instance, even a slightly worse S/N ratio in the top spectrum of Fig. S1 would preclude an unambiguous detection of the signal from Q^1_{P} groups, despite that their identification is much less problematic in BGs exhibiting higher silicate network connectivities and thereby increased x^1_{P}-values. The relative Q^1_{P} fraction is sufficiently low in the 45S5 glass structure that neither ^{31}P NMR on static powders nor ^{17}O triple-quantum MAS[S4] experimentation allowed its detection.[S3] Yet, static ^{31}P NMR is expected to detect Q^1_{P} groups if they are present in larger amounts, such for BGs featuring $\overline{N}^{\mathrm{Si}}_{\mathrm{BO}} \geqslant 2.5$.

A few of the current ^{31}P NMR spectra were presented previously by us;[S5] we then invoked signal contributions from both Q^0_{P} and Q^1_{P} groups in the iterative fitting throughout, except for that of the $\mathrm{BG}_{2.6}(2.1)$ composition. However, we should also then have considered a two-peak fit comprising the very minor Q^1_{P} contribution. Figure S2 displays the difference between employing deconvolutions into one and two NMR peaks of the spectra from the two $\mathrm{BG}_{2.6}(2.1)$ and $\mathrm{BG}_{6.0}(2.1)$ samples: it shows that by using two peak components, the deviations between the experimental and best-fit spectra reduce markedly.

S1.2 ^{31}P Chemical Shifts *versus* Na^+/Ca^{2+}–PO_4^{3-} Contacts: Further Discussion

The ^{31}P chemical shifts listed in Table 2 were obtained from glasses featuring either increasing P contents at constant $\overline{N}_{BO}^{Si}$ (see Fig. 1) or variable $\overline{N}_{BO}^{Si}$-values at nearly fixed P contents (see Fig. 2). From their absence of significant variations, thereby suggesting very similar Na/Ca constellations around the Q_P^0 and Q_P^1 environments, we infer essentially statistically distributed modifiers around P, as also concluded by previous ^{31}P NMR investigations.[S6–S10] Yet, there may be some minor deviations from such a scenario: the $\{\delta_P^n\}$ data of Table 1 reveals a small but consistent peak-shift by around -1 ppm when the $\overline{N}_{BO}^{Si}$-value increases from 2.5 to 2.9, suggesting that there may be a slight preference for phosphate-association with Ca^{2+} rather than Na^+ cations in structures exhibiting a high silicate network connectivity. This is probably also the origin behind the unexpectedly low shift $\delta_P^0 = 7.5$ ppm observed from the comparatively Na-*rich* $BG_{2.6}(2.7)$ structure. The anticipated ^{31}P chemical-shift increase from the slightly higher Na content is likely counteracted by the shift-decrease stemming from a larger number of Ca–P contacts relative to Na–P; compare, for instance, with the shift $\delta_P^0 = 8.7$ ppm observed from $BG_{2.6}(2.1)$ that exhibits an equal n_{Na}/n_{Ca} ratio but a lower silicate network connectivity of $\overline{N}_{BO}^{Si} = 2.1$. Given that the present ^{31}P chemical-shift based analysis is only qualitative, more conclusive experimental investigations are underway for gaining further insight into the relative Na/Ca–Si/P associations, the results of which will be presented elsewhere.

S2 ^{29}Si NMR

Owing to their larger number of overlapping peak components, deconvolutions of the ^{29}Si NMR spectra are significantly less reliable than those for ^{31}P, and they do not generally admit reliable results by unconstrained fitting. We normally employ (δ, W) parameters restricted within a few ppm,[S2,S11,S12] as in the present case of ^{31}P. Here, however, all Q_{Si}^n peak positions, as well as the fwhm values, were highly constrained within ± 0.25 ppm. For each glass series of constant $\overline{N}_{BO}^{Si}$, its "representative" $\{\delta_{Si}^n, W_{Si}^n\}$ values were located by an initial, loosely constrained iterative parameter fitting (as in section S1.1). These pairs of "typical" $\{\delta_{Si}^n, W_{Si}^n\}$ values were then only allowed to vary within ± 0.25 ppm during the second deconvolution stage of each $BG(\overline{N}_{BO}^{Si})$ glass series.

This procedure does not permit an accurate assessment of the uncertainty of each best-fit parameter $\{\delta_{Si}^n, W_{Si}^n, x_{Si}^n\}$, where the *unconstrained* fractional populations $\{x_{Si}^n\}$ constitute the primary targets. Nevertheless, the following consistency-checks are gratifying: (*i*) Within each BG(2.5) and BG(2.9) series, essentially identical ^{29}Si NMR spectra are observed (except for those of $BG_{1.0}(2.5)$ and $BG_{3.0}(2.9)$ that are commented below). As then *required*, the deconvolution output verify nearly equal $\{x_{Si}^n\}$ sets (Table 3). (*ii*) Further support for the validity of the best-fit x_{Si}^n values are provided from the good agreement between the nominal $\{\overline{N}_{BO}^{Si}\}$ sets and their ^{29}Si NMR-derived counterparts obtained from Eq. (3).

It has been recommended that the $\overline{N}_{BO}^{Si}$-value should be involved as a direct constraint among the $\{x_{Si}^n\}$ populations during the iterative fitting.[S3] However, this assumes/requires that the nominal and physical glass compositions are indeed identical, whereas if they are not, systematic errors are introduced in the output fractional populations. Hence, we merely employ the $\overline{N}_{BO}^{Si}$(nom) values as an *independent* quality check of the best-fit data.

Each of the two BG(2.5) and BG(2.9) glass series reveals one "outlier" sample (see Fig. 3). Given that the ^{29}Si NMR spectrum from each of these deviate slightly from the rest within each series, this must be reflected by slightly different $\{Q_{Si}^n\}$ best-fit sets, as indeed witnessed by the respective results of Table 3. The best-fit $\{x_{Si}^n\}$ populations obtained from the $BG_{1.0}(2.5)$ glass reveal higher (lower) x_{Si}^2 (x_{Si}^3) values than the other BG(2.5) specimens, whereas a higher

Q^2_{Si} population is observed for $BG_{3.0}(2.9)$ compared to the remaining of the BG(2.9) branch. These ^{29}Si NMR observations suggest that there may be minor differences between the prepared glass compositions and their respective batched (nominal) counterparts for the $BG_{1.0}(2.5)$ and $BG_{3.0}(2.9)$ glasses.

Note that there are minor Q^1_{Si} moieties present in all glasses associated with $\overline{N}^{Si}_{BO} \leq 2.5$, whereas the Q^4_{Si} populations are non-negligible throughout those featuring $\overline{N}^{Si}_{BO} \geq 2.5$. While the Q^1_{Si}/Q^4_{Si} species remain very low in some structures, their consideration consistently improved the quality of the spectra deconvolutions. However, unless the NMR data exhibit very high S/N (for the present spectra in the range 300-450), it is difficult to justify the inclusion of peak components whose populations amount to only a few percent ($\lesssim 5\%$) of the total SiO_4 speciation (as in the analogous scenario of Q^1_P groups *without* additional information), and thereby establishing deviations from a strict binary BO/NBO distribution scenario. A widely spanning quality of the experimental data is likely the primary reason for the somewhat different inferences emerging from various ^{29}Si NMR studies about the nature of the BO/NBO-distribution among the SiO_4 groups in silicate glasses; see section 4.3.2.

S3 MD Simulations

Table S1 specifies the number of simulated atoms and lists the $\{Q^n_P\}$ and $\{Q^n_{Si}\}$ populations (including the extremely low fractions of Q^2_P groups not presented in Table 4) obtained from each of the 2-4 independent simulations per sample. Note that glass compositions featuring low P_2O_5 contents (<3 mol-%) generally used a larger number of 10^4 atoms, whereas those richer in P employed ≈6000 atoms. This approach reduced some data scatter of the $\{x^0_P, x^1_P\}$ populations stemming from using a (too) small number of P atoms. Across the entire set of BG compositions, the standard deviations of the x^1_P values among distinct simulations of a given composition consistently remained below 0.05, with the result σ=0.034 obtained for the standard deviation taken across the entire set of samples/configurations that involved ≈6000 atoms. Simulations based on less than 10^4 atoms revealed a significantly higher scatter among the configurations of glass compositions associated with $x(P_2O_5)$<0.03; several additional modeled results that were performed for systems comprising <6000 atoms are neither included in our analysis nor shown in Table S1.

Besides the number of simulated atoms, the convergence of the Q^n_P fractional populations may be affected by the fast cooling rate (q_C),[S13,S14] which is $\sim 10^{10}$ times faster in the calculations than that involved in the glass synthesis. The present value of $q_C = 10$ K/ps is commonly employed in MD work on related BG systems;[S3,S15-S17] we selected it as a compromise between realistic computation times but avoiding a too small number of atoms per simulation (as discussed above), ensuring further reliability by performing 2-4 separate simulations, as well as allowing the probing of a large series of 13 glasses. The cooling-rate dependence of the x^1_P populations of 45S5 was very recently explored by Tilocca over a large range of q_C-values,[S14] where significant variations of the simulated x^1_P populations were only observed for $q_C > 5$ K/ps. Incidentally, the present value $x^1_P = 0.166$ for the same glass composition and $q_C = 10$ K/ps is very close to the result reported for $q_C = 5$ K/ps in ref. S14.

To explore the potential cooling-rate effects on the phosphate speciations of the present glasses, simulations of the $BG_{6.0}(2.5)$ and $BG_{2.0}(2.5)$ compositions were performed with 5644 and 5768 atoms, respectively (see Table S1). In the former case, the Q^1_P population varied slightly against the quench-rate as follows: 0.332 (20 K/ps), 0.304 (10 K/ps), 0.258 (5 K/ps), and 0.276 (2 K/ps); while the slight initial x^1_P decrease between 20 and 5 K/ps confirms the general trend highlighted in ref. S14, the deviations between the result at $q_C = 10$ K/ps and those obtained at other cooling rates remain small and comparable with the standard deviation associated with simply using distinct different initial configurations of otherwise identical simulations ($\sigma = 0.034$;

see comments above). For the case of $BG_{2.0}(2.5)$, only two additional calculations were carried out with $q_C = 20$ K/ps and $q_C = 5$ K/ps, yielding $x_P^1 = 0.262$ and $x_P^1 = 0.275$, which may be contrasted with the very similar result of $x_P^1 = 0.267$ for $q_C = 10$ K/ps (see Table S1). Altogether, these variations are well within the stated uncertainty of our simulated $\{x_P^0,\ x_P^1\}$ values. We also note that the $\{Q_{Si}^n\}$ populations did not reveal any trends (or significant variations) when the quench-rate varied.

Table S1: MD-derived fractional populations of $Q^n_{\mathbf{P}}$ and $Q^n_{\mathbf{Si}}$ groups[a]

Sample label	N_{tot}[b]	N_{P}[b]	N_{Si}[b]	Q^n_{P} populations			Q^n_{Si} populations					$\overline{N}^{\mathrm{Si}}_{\mathrm{BO}}$(MD)
				x^0_{P}	x^1_{P}	x^2_{P}	x^0_{Si}	x^1_{Si}	x^2_{Si}	x^3_{Si}	x^4_{Si}	
$BG_{2.6}(2.1)$	10017	184	1632	**0.834**	**0.166**	**0.000**	**0.011**	**0.186**	**0.517**	**0.266**	**0.021**	**2.102**
				0.826	0.174	0.000	0.008	0.187	0.526	0.254	0.025	2.101
				0.842	0.158	0.000	0.013	0.184	0.508	0.277	0.018	2.103
$BG_{6.0}(2.1)$	6123	252	829	**0.798**	**0.200**	**0.002**	**0.010**	**0.197**	**0.514**	**0.252**	**0.027**	**2.090**
				0.790	0.210	0.000	0.010	0.199	0.514	0.248	0.029	2.088
				0.806	0.190	0.004	0.010	0.195	0.514	0.256	0.025	2.091
$BG_0(2.5)$	5516	0	1144	–	–	–	**0.003**	**0.068**	**0.428**	**0.425**	**0.076**	**2.503**
				–	–	–	0.003	0.069	0.426	0.427	0.075	2.503
				–	–	–	0.003	0.067	0.431	0.422	0.077	2.503
$BG_{1.0}(2.5)$	12279	88	2416	**0.670**	**0.318**	**0.011**	**0.001**	**0.073**	**0.426**	**0.435**	**0.065**	**2.491**
				0.636	0.352	0.011	0.001	0.072	0.428	0.436	0.063	2.490
				0.705	0.284	0.011	0.001	0.074	0.424	0.434	0.067	2.492
$BG_{2.0}(2.5)$	5768	80	1076	**0.721**	**0.267**	**0.013**	**0.002**	**0.080**	**0.418**	**0.440**	**0.060**	**2.476**
				0.725	0.250	0.025	0.001	0.085	0.416	0.434	0.064	2.475
				0.713	0.287	0.000	0.005	0.081	0.411	0.440	0.063	2.477
				0.725	0.263	0.013	0.001	0.074	0.427	0.444	0.054	2.477
$BG_{4.0}(2.5)$	6280	176	1044	**0.622**	**0.364**	**0.014**	**0.002**	**0.084**	**0.442**	**0.409**	**0.063**	**2.447**
				0.585	0.398	0.017	0.000	0.086	0.452	0.396	0.065	2.440
				0.608	0.369	0.023	0.001	0.078	0.459	0.402	0.060	2.443
				0.625	0.375	0.000	0.002	0.088	0.424	0.429	0.057	2.449
				0.670	0.313	0.017	0.003	0.085	0.435	0.408	0.069	2.455
$BG_{6.0}(2.5)$	5644	232	828	**0.690**	**0.304**	**0.006**	**0.002**	**0.087**	**0.457**	**0.392**	**0.062**	**2.423**
				0.681	0.319	0.000	0.004	0.092	0.448	0.391	0.065	2.422
				0.698	0.289	0.013	0.001	0.082	0.466	0.392	0.058	2.424
$BG_{2.6}(2.7)$	9999	180	1909	**0.517**	**0.475**	**0.008**	**0.001**	**0.041**	**0.336**	**0.507**	**0.115**	**2.695**
				0.494	0.500	0.006	0.001	0.043	0.337	0.499	0.120	2.693
				0.539	0.450	0.011	0.001	0.039	0.334	0.516	0.111	2.697
$BG_0(2.9)$	5606	0	1304	–	–	–	**0.000**	**0.016**	**0.225**	**0.571**	**0.189**	**2.932**
				–	–	–	0.000	0.015	0.229	0.564	0.192	2.932
				–	–	–	0.000	0.016	0.221	0.577	0.186	2.932
$BG_{2.0}(2.9)$	6080	88	1272	**0.417**	**0.553**	**0.030**	**0.001**	**0.017**	**0.246**	**0.553**	**0.183**	**2.901**
				0.364	0.614	0.023	0.001	0.019	0.248	0.546	0.186	2.898
				0.409	0.557	0.034	0.000	0.015	0.252	0.550	0.182	2.900
				0.478	0.488	0.034	0.001	0.018	0.237	0.563	0.181	2.905
$BG_{3.0}(2.9)$	6081	126	1205	**0.445**	**0.528**	**0.028**	**0.000**	**0.020**	**0.252**	**0.562**	**0.166**	**2.872**
				0.452	0.500	0.048	0.001	0.020	0.263	0.540	0.176	2.870
				0.437	0.556	0.008	0.000	0.021	0.241	0.583	0.155	2.873
$BG_{4.0}(2.9)$	6372	176	1192	**0.440**	**0.554**	**0.006**	**0.000**	**0.022**	**0.269**	**0.539**	**0.169**	**2.856**
				0.438	0.557	0.006	0.000	0.019	0.270	0.549	0.163	2.856
				0.443	0.551	0.006	0.000	0.026	0.268	0.530	0.176	2.856
$BG_{6.0}(2.9)$	6000	240	996	**0.460**	**0.527**	**0.012**	**0.000**	**0.028**	**0.295**	**0.529**	**0.149**	**2.799**
				0.433	0.554	0.013	0.000	0.028	0.296	0.531	0.145	2.792
				0.488	0.500	0.012	0.000	0.027	0.293	0.527	0.153	2.805

[a]Bold-face entries correspond to the fractional populations listed in Table 4; they represent averages over the individual data listed beneath.

[b]N_{tot} represents the total number of atoms in the simulation, whereas N_{P} and N_{Si} correspond to those of P and Si, respectively.

References

(S1) MacKenzie, K. J. D.; Smith, M. E., Multinuclear Solid-State NMR of Inorganic Materials, Pergamon Press: Amsterdam, 2002.

(S2) Leonova, E.; Izquierdo-Barba, I.; Arcos, D.; Lopez-Noriega, A.; Hedin, N.; Vallet-Regí, M.; Edén, M., Multinuclear Solid-State NMR Studies of Ordered Mesoporous Bioactive Glasses *J. Phys. Chem. C* **2008**, *112*, 5552–5562.

(S3) Pedone, A.; Charpentier, T.; Malavasi, G.; Menziani, M. C., New Insights into the Atomic Structure of 45S5 Bioglass by Means of Solid-State NMR Spectroscopy and Accurate First-Principles Simulations *Chem. Mater.* **2010**, *22*, 5644–5652.

(S4) Frydman, L.; Harwood, J. S., Isotropic Spectra of Half-Integer Quadrupolar Spins from Bidimensional Magic-Angle-Spinning NMR *J. Am. Chem. Soc.* **1995**, *117*, 5367–5368.

(S5) Mathew, R.; Turdean-Ionescu, C.; Stevensson, B.; Izquierdo-Barba, I.; García, A.; Arcos, D.; Vallet-Regí, M.; Edén, M., Direct Probing of the Phosphate-Ion Distribution in Bioactive Silicate Glasses by Solid-State NMR: Evidence for Transitions between Random/Clustered Scenarios *Chem. Mater.* **2013**, *25*, 1877–1885.

(S6) Lockyer, M. W. G.; Holland, D.; Dupree, R., NMR Investigation of the Structure of some Bioactive and Related Glasses *J. Non-Cryst. Solids* **1995**, *188*, 207–219.

(S7) Grussaute, H.; Montagne, L.; Palavit, G.; Bernard, J. L., Phosphate Speciation in Na_2O–CaO–P_2O_5–SiO_2 and Na_2O–TiO_2–P_2O_5–SiO_2 Glasses *J. Non-Cryst. Solids* **2000**, *263*, 312–317.

(S8) Elgayar, I.; Aliev, A. E.; Boccaccini, A. R.; Hill, R. G., Structural Analysis of Bioactive Glasses *J. Non-Cryst. Solids* **2005**, *351*, 173–183.

(S9) FitzGerald, V.; Pickup, D. M.; Greenspan, D.; Sarkar, G.; Fitzgerald, J. J.; Wetherall, K. M.; Moss, R. M.; Jones, J. R.; Newport, R. J. A Neutron and X-ray Diffraction Study of Bioglass® with Reverse Mote-Carlo Modelling *Adv. Funct. Mater.* **2007**, *17*, 3746–3753.

(S10) O'Donnell, M. D.; Watts, S. J.; Law, R. V.; Hill, R. G., Effect of P_2O_5 Content in Two Series of Soda Lime Phosphosilicate Glasses on Structure and Properties–Part I: NMR *J. Non-Cryst. Solids* **2008**, *354*, 3554–3560.

(S11) Gunawidjaja, P. N.; Lo, A. Y. H.; Izquierdo-Barba, I.; García, A.; Arcos, D.; Stevensson, B.; Grins, J.; Vallet-Regí, M.; Edén, M., Biomimetic Apatite Mineralization Mechanisms of Mesoporous Bioactive Glasses as Probed by Multinuclear ^{31}P, ^{29}Si, ^{23}Na and ^{13}C Solid State NMR *J. Phys. Chem. C* **2010**, *114*, 19345–19356.

(S12) Gunawidjaja, P. N.; Mathew, R.; Lo, A. Y. H.; Izquierdo-Barba, I.; García, A.; Arcos, D.; Vallet-Regí, M.; Edén, M., Local Structures of Mesoporous Bioactive Glasses and Their Surface Alterations *In Vitro*: Inferences from Solid State Nuclear Magnetic Resonance *Phil. Trans. R. Soc. A* **2012**, *370*, 1376–1399.

(S13) Du, J.; Xiang, Y., Effect of Strontium Substitution on the Structure, Ionic Diffusion and Dynamic Properties of 45S5 Bioactive Glasses *J. Non-Cryst. Solids* **2012**, *358*, 1059–1071.

(S14) Tilocca, A., Cooling Rate and Size Effects on the Medium-Range Structure of Multicomponent Oxide Glasses Simulated by Molecular Dynamics *J. Chem. Phys.* **2013**, *139*, 114501.

(S15) Tilocca, A.; Cormack, A. N., Structural Effects of Phosporus Inclusion in Bioactive Silicate Glasses *J. Phys. Chem. B* **2007**, *111*, 14256–14264.

(S16) Tilocca, A.; Cormack, A. N.; de Leeuw, N. H., The Structure of Bioactive Silicate Glasses: New Insight from Molecular Dynamics Simulations *Chem. Mater.* **2007**, *19*, 95–103.

(S17) Pedone, A.; Malavasi, G.; Menziani, M. C., Computational Insight into the Effect of CaO/MgO Substitution on the Structural Properties of Phospho-Silicate Bioactive Glasses *J. Phys. Chem. C* **2009**, *113*, 15723–15730.

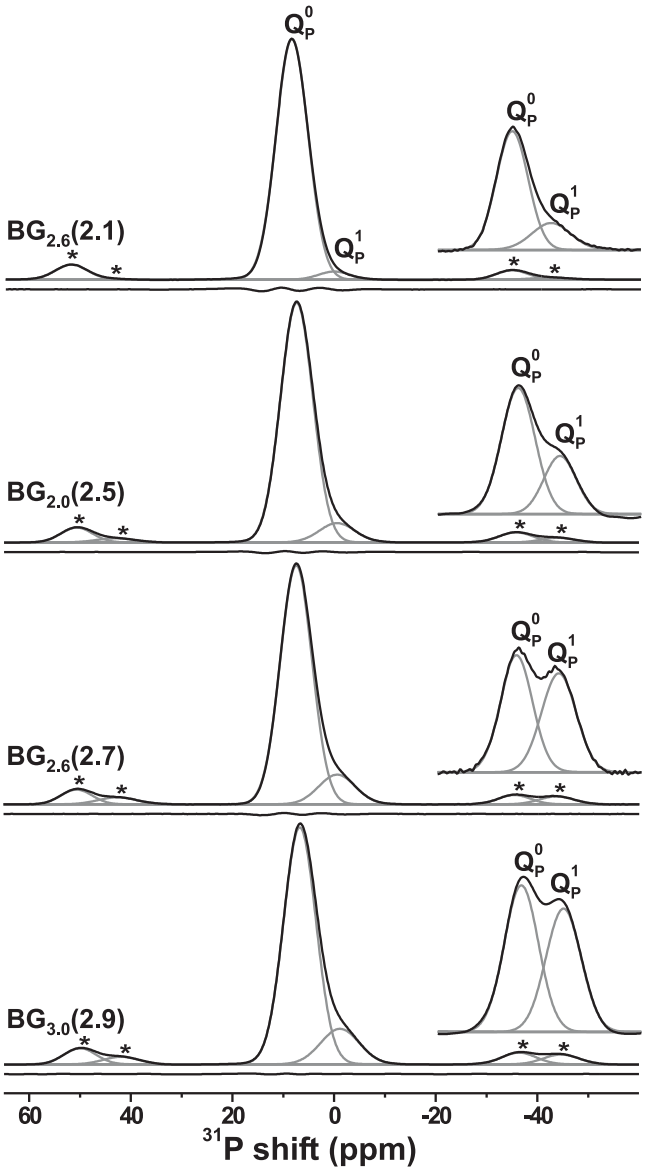

Figure S1. Experimental ^{31}P NMR data (black traces), displayed over a larger spectral range to reveal the weak spinning sideband contributions (marked by asterisks). The Q^0_{P} and Q^1_{P} signal components (grey traces) resulting from deconvolution are also displayed. The curve beneath each spectrum reveals the difference between the experimental and best-fit spectrum. Note that each spinning sideband comprises a relatively stronger signal intensity from Q^1_{P} groups compared to that of the centerband, which is dominated by the Q^0_{P} NMR signal. Besides assisting the detection of the ^{31}P resonances from Q^1_{P} groups, this feature was utilized to locate the isotropic chemical shift δ^1_{P} at the centerband and thereby better constrain this parameter in the iterative fitting procedure.

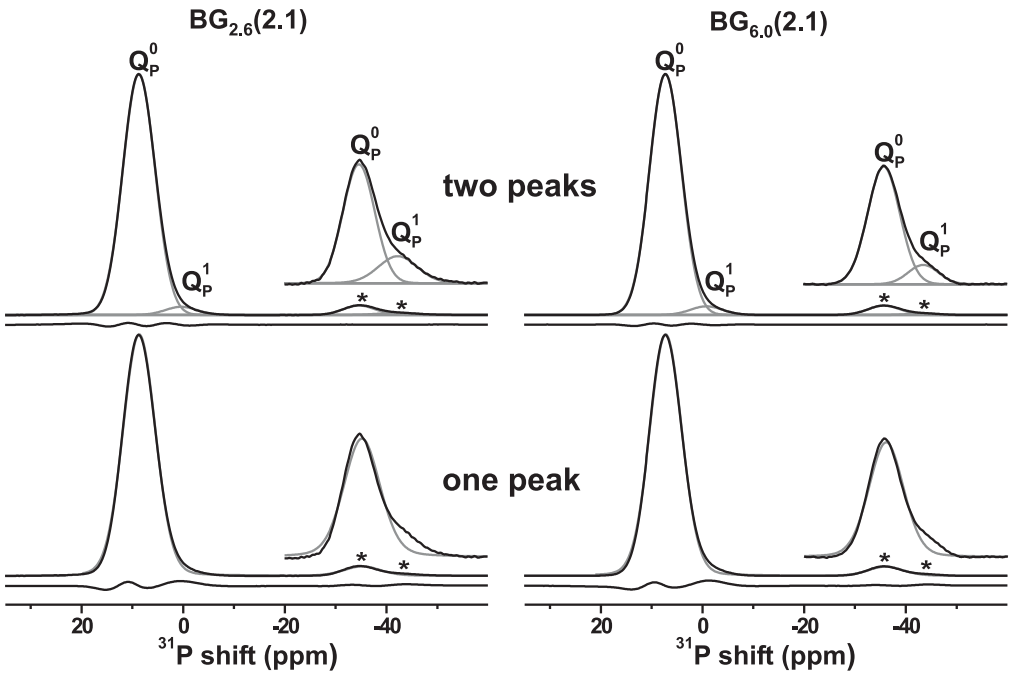

Figure S2. Experimental ^{31}P NMR spectra from the $BG_{2.6}(2.1)$ [left panel] and $BG_{6.0}(2.1)$ [right panel] glasses, deconvoluted into either two peaks (top row) from Q^0_P and Q^1_P groups, or solely one peak from the Q^0_P groups (bottom row). Note the significantly improved quality of the two-peak fits, reflected by their reduced discrepancy between the experimental and best-fit results revealed by the curve beneath each NMR spectrum.